

UC Berkeley

UC Berkeley Previously Published Works

Title

Anomalous transient enhancement of planetary ion escape at Mars.

Permalink

<https://escholarship.org/uc/item/55t1p2pg>

Journal

Nature Communications, 16(1)

Authors

Zhang, Chi

Dong, Chuanfei

Zhou, Hongyang

et al.

Publication Date

2025-04-02

DOI

10.1038/s41467-025-58351-y

Peer reviewed

Anomalous transient enhancement of planetary ion escape at Mars

Received: 19 September 2024

Accepted: 17 March 2025

Published online: 02 April 2025

 Check for updates

Chi Zhang ¹✉, Chuanfei Dong ¹✉, Hongyang Zhou ¹, Jasper Halekas ², Masatoshi Yamauchi ³, Hans Nilsson ³, Terry Z. Liu ⁴, Moa Persson ⁵, Shannon Curry ⁶, Yaxue Dong ⁶, Yoshifumi Futaana ³, Yuxi Chen ⁷, Muni Zhou ⁸, Ruhunusiri Suranga ⁶, Kathleen G. Hanley ⁹, Christian Mazelle ¹⁰, Shaosui Xu ⁹, Robin Ramstad ⁶, Mats Holmström ³ & Li-Jen Chen ¹¹

Atmospheric ion escape plays a crucial role in the evolution of planetary climate and habitability. While Mars has been the focus of extensive in-situ spacecraft observations, our understanding of ion escape at Mars has been constrained by single-point spacecraft measurements, which fail to distinguish spatial and temporal variability. Observations from NASA's Mars Atmosphere and Volatile Evolution (MAVEN) mission and China's Tianwen-1 mission provide complementary observations the Martian space environment and a unique opportunity to study the variability of ion escape. Here, we report that ion escape at Mars exhibits unexpected spatial-temporal variability under steady and weak external solar wind conditions. In the hemisphere where the solar wind electric field is directed toward the planet, a condition that usually hinders ion escape into space, we instead observe the transient appearance of escaping planetary ions with high energies and strong escape fluxes. This finding underscores that planetary ion escape can be unsteady and dynamic, even under stable external conditions.

Mars has always been an important target in planetary science due to its divergent evolution from Earth. Ancient Mars is believed to have had a global dipole magnetic field, a thick atmosphere, and surface liquid water, similar to present-day Earth^{1–3}. However, modern Mars lacks both a global dipole magnetic field and surface liquid water, possessing only a tenuous, CO₂ (carbon dioxide)-dominated atmosphere. This suggests that Mars has undergone significant atmospheric loss. An important factor contributing to this loss is the absence of a global dipole magnetic field, which allows the solar wind (a high-speed stream of charged particles emitted from the Sun) to directly strip away the upper Martian atmosphere and facilitate the escape of

atmospheric ions into space^{4–16}. Consequently, understanding how the solar wind energizes planetary ions and drives their escape is essential for comprehending the long-term atmospheric evolution of Mars, its climate change, and its potential habitability.

When the solar wind encounters Mars, the solar wind plasma and “frozen-in” interplanetary magnetic field (IMF) generate a motional electric field (E_{SW}) in the Mars rest frame. This electric field initially accelerates the ionospheric ions, primarily O⁺ (oxygen ions) and O₂⁺ (molecular oxygen ions), along its direction and subsequently deflects the ions anti-sunward. As a result, in the hemisphere where E_{SW} points away from the planet, called +E hemisphere, the ions gradually gain

¹Center for Space Physics and Department of Astronomy, Boston University, Boston, MA, USA. ²Department of Physics and Astronomy, University of Iowa, Iowa City, IA, USA. ³Swedish Institute of Space Physics, Kiruna, Sweden. ⁴Department of Earth, Planetary, and Space Sciences, University of California, Los Angeles, CA, USA. ⁵Swedish Institute of Space Physics, Uppsala, Sweden. ⁶Laboratory for Atmospheric and Space Physics, University of Colorado, Boulder, CO, USA. ⁷Department of Climate and Space Sciences and Engineering, University of Michigan, Ann Arbor, MI, USA. ⁸Department of Physics and Astronomy, Dartmouth College, Hanover, NH, USA. ⁹Space Sciences Laboratory, University of California, Berkeley, Berkeley, CA, USA. ¹⁰IRAP, Université de Toulouse, CNRS, UPS CNES, Toulouse, France. ¹¹NASA Goddard Space Flight Center, Greenbelt, MD, USA. ✉e-mail: zc199508@bu.edu; dcfy@bu.edu

energy as they ascend from the ionosphere¹⁷. Thus, the ions have a high probability of becoming highly energized and escaping into space^{18,19}. These escaping and energized ions form a plume extending from the low-altitude ionosphere beyond the bow shock, contributing about 20%–30% to the total escape rate of ions^{20–24}. Conversely, in the -E hemisphere where \mathbf{E}_{SW} points toward the planet, the dayside ionospheric ions are accelerated back toward the planet, causing many of these ions to return to the atmosphere instead of escaping to space¹⁹.

However, the current understanding of ion escape at Mars has primarily relied on single-point measurements, which fall short in distinguishing the spatial and temporal variations. Previous studies have demonstrated that ion escape at Mars can exhibit a bursty signature, marked by considerable transient enhancements in escaping ion flux^{13,25,26}. It has been suggested that such bursty escape of ionospheric ions may be triggered by crustal field reconnection²⁵ or the snowplow effect at the boundary²⁷. Nonetheless, the actual solar wind conditions during these bursty escape events were unknown. Consequently, it remains uncertain whether these events are triggered by the temporal variations of external solar wind or by other sources. Additionally, it is uncertain whether these events are global or localized phenomena. Notably, even under conditions of constant solar wind, its interaction with the bow shock can naturally introduce various waves and coherent, spatially localized structures in the foreshock region^{28,29}. These structures, which introduce additional inhomogeneities in the solar wind, could also directly interact with the ionosphere, potentially introducing further temporal-spatial variabilities to the escaping of ions. However, the specific impacts of these inhomogeneities remain poorly understood. Addressing these gaps is crucial for advancing our understanding of planetary ion escape, necessitating the deployment of multi-point spacecraft missions. To this end, multi-point spacecraft missions such as NASA's ESCAPE³⁰, and ESA's M-MATISSE mission³¹ have been proposed. Fortunately, NASA's MAVEN (Mars Atmosphere and Volatile Evolution)³² and China's Tianwen-1³³ are contemporaneously measuring the magnetic fields and ion properties at Mars. This situation offers two-point measurements and provides a unique opportunity to explore the temporal and spatial variability of ion escape, of particular interest to future multi-point spacecraft missions.

Here, we show that ion escape at Mars exhibits anomalous temporal and spatial variability under steady external conditions, based on concurrent observations from MAVEN and Tianwen-1. This finding underscores that the interaction between the solar wind and Mars, as well as ion escape, are far more complex and dynamic than previously thought, highlighting the need for further multi-point observations.

Results

Event overview

During 13:24–13:29 UTC, September 23, 2022, both the MAVEN and Tianwen-1 were located in the terminator region of Mars (see Fig. 1a). The average location of MAVEN was $(-0.191, -1.415, 1.817) R_M$ (radius of Mars, $R_M = 3390$ km) in the Mars Solar Orbital (MSO, see Methods subsection MSO and MSE Coordinates) coordinates, placing it near the location of nominal bow shock (refer to Fig. 1a). Tianwen-1's average location was roughly $(0.057, -1.473, -0.242) R_M$, indicating its proximity to the nominal magnetic pile-up boundary (see Methods subsection Magnetic Pile-up Boundary) (refer to Fig. 1a, b).

Figure 1c–h shows the overview of this event. During this time interval, MAVEN consistently detected shocked solar wind H^+ with energies ranging from approximately 50 eV to 2 keV (see Fig. 1c), indicating that MAVEN was in the magnetosheath. Between 13:26:00 and 13:27:30 marked by the grey shaded interval in Fig. 1c–h, MAVEN recorded the depletion of H^+ , and sudden appearance of a group of energetic O^+ (see Fig. 1d) and O_2^+ (see Fig. 1e) with energy spanning from 1 keV to 5 keV. Figure 1f reveals that the number density of O_2^+ and O^+ surged to approximately 6 cm^{-3} and 3 cm^{-3} , respectively, while the density of H^+ fell below 1 cm^{-3} . Supplementary Fig. 1 further demonstrates that these heavy

ions are primarily composed of O_2^+ and O^+ . The presence of such a dense O_2^+ indicates that these oxygen ions originate from the ionosphere rather than the exosphere²³. These ionospheric ions exhibit a significant tailward escape velocity (see Fig. 1g), with O^+ traveling at approximately 149.3 km/s and O_2^+ at around 118.3 km/s. Based on the observed density and tailward speed, we estimate the average escaping flux of O^+ and O_2^+ to be about $1.23 \times 10^7 \text{ cm}^{-2} \text{ s}^{-1}$ and $2.38 \times 10^7 \text{ cm}^{-2} \text{ s}^{-1}$, respectively. In comparison, the average escape flux in the magnetotail is around $1.2 \times 10^6 \text{ cm}^{-2} \text{ s}^{-1}$ ^{4,10,34}, while the average escape flux in the dayside plume in the +E hemisphere is about $3.6 \times 10^5 \text{ cm}^{-2} \text{ s}^{-1}$ ²⁰. Thus, the observed transient ions represent a bursty enhancement of ionospheric ion escape, with fluxes one or two orders of magnitude higher than those in the nightside magnetotail or dayside plume.

During this event, STATIC's field of view did not vary during this interval, effectively ruling out instrumental artifacts (see Supplementary Fig. 2). In the orbit preceding this event, MAVEN recorded similar magnetosheath characteristics as in the orbit during the event (refer to Supplementary Fig. 3). This consistency suggests that the external solar wind conditions remained relatively unchanged between these orbits. Additionally, the absence of high-energy ionospheric ions in the earlier orbit indicates their transient nature. For both orbits, MAVEN's trajectory extended beyond the nominal bow shock position, yet it did not cross the bow shock in either case (see Supplementary Fig. 4). This suggests that the external solar wind was weaker than typically observed under normal conditions.

Analysis of the magnetic field

Alongside the presence of ionospheric ions, the magnetic fields exhibited notable fluctuations (see Fig. 1h), clearly distinguishable from the steady magnetic fields in the background magnetosheath. However, upon examining Fig. 2a, b, which compare the magnetic fields observed by MAVEN and Tianwen-1, we observe that Tianwen-1 detected no disturbances in the magnetic fields throughout the entire duration, suggesting that the magnetic field fluctuation is spatially localized, rather than being a global phenomenon. Furthermore, the long-lasting, steady magnetic fields observed by Tianwen-1 also indicate that the solar wind conditions were relatively stable during this event. Otherwise, the global configuration of the induced magnetosphere would rapidly alter in response to changes in solar wind conditions^{13,35–37}. Therefore, we conclude that MAVEN detected transient, burst-like enhancements in the escape of high-energy ionospheric ions under conditions of relatively stable solar wind.

Generally, these energetic ionospheric ions with significant escaping velocity and flux are observed in the +E hemisphere, since the solar wind electric fields point away from the planet²⁰. To check this, we construct the Mars Solar Electric coordinates (MSE, see “Methods” subsection “MSO and MSE Coordinates”). Although neither MAVEN nor Tianwen-1 provide direct measurements of the upstream IMF, the clock angle of magnetic fields measured in the downstream region can serve as a proxy for the clock angle of the upstream IMF^{38,39}. The clock angle, ϕ , is defined as the angle between the projected magnetic fields and \mathbf{Z}_{MSO} in the $Y_{\text{MSO}} - Z_{\text{MSO}}$ plane, with the angle rotationally increasing from $+\mathbf{Z}_{\text{MSO}}$ toward $+\mathbf{Y}_{\text{MSO}}$. Hence, $\phi = 90^\circ$ (or 270°) indicates that the projected magnetic field points toward $+\mathbf{Y}_{\text{MSO}}$ (or $-\mathbf{Y}_{\text{MSO}}$). From Fig. 2c, we see that, except for a brief period during 13:25:58–13:26:06 (see the yellow shaded interval in Fig. 2a–c), the clock angles of the magnetic fields recorded by both MAVEN and Tianwen-1 were comparable, with MAVEN registering a clock angle of 233° and Tianwen-1 at 212° . Consequently, we consider the average clock angle of the magnetic fields measured by MAVEN and Tianwen-1, -228.5° , as representative of the clock angle of upstream IMF. We also referenced upstream IMF values determined through the artificial neural network (ANN) approach⁴⁰, which are $(1.82, -1.81, -1.03)$ nT, with a clock angle of 240° . This is also close to the clock angles measured by MAVEN and Tianwen-1, lending confidence to this method.

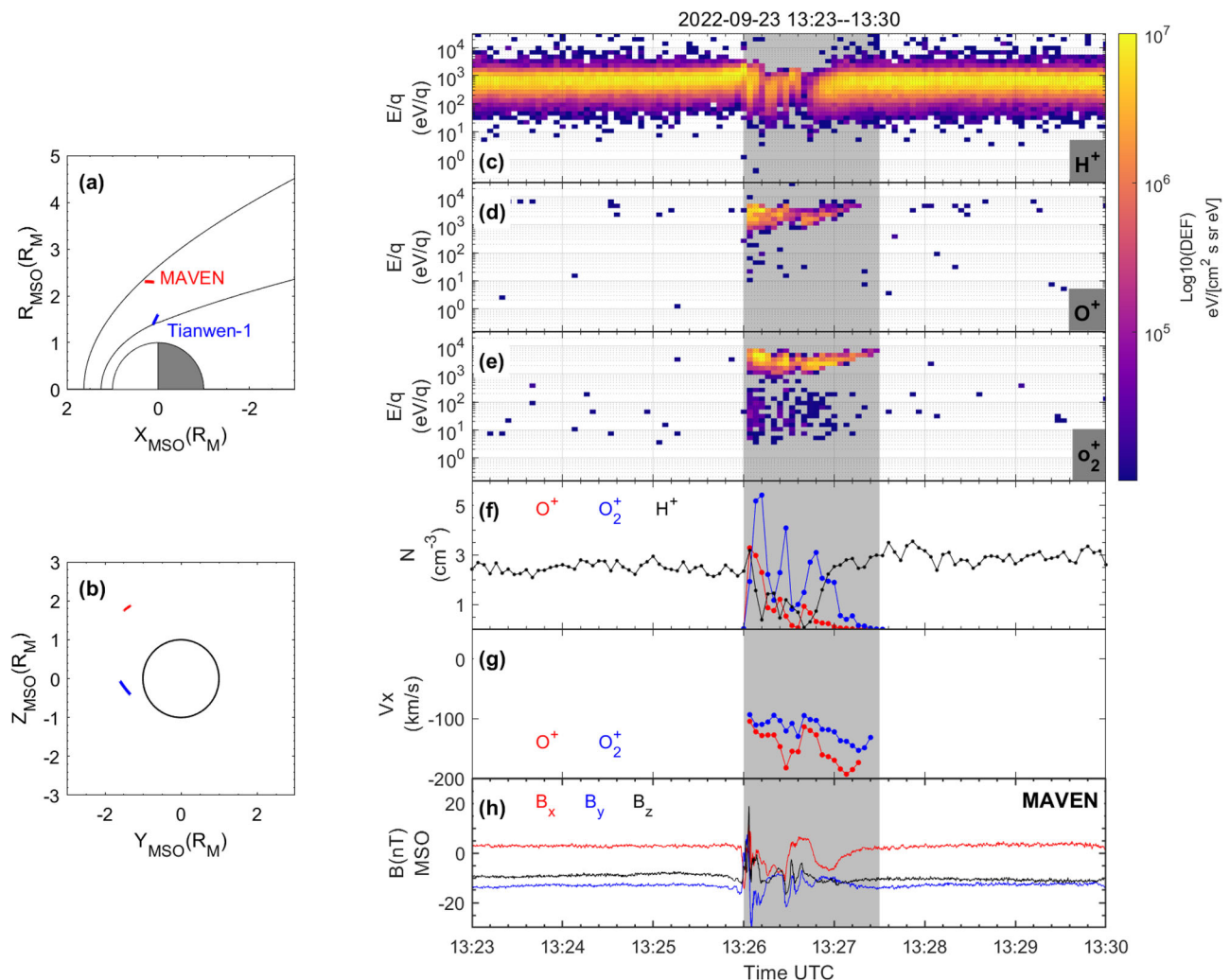


Fig. 1 | Overview of the case occurred on September 23, 2022. **a** Shows the positions of MAVEN and Tianwen-1 in the $X_{MSO} - R_{MSO}$ plane, where $R = \sqrt{Y_{MSO}^2 + Z_{MSO}^2}$. The black dashed curves represent the nominal bow shock and magnetic pile-up boundary (MPB)⁶⁷. **b** Shows the locations of the MAVEN and Tianwen-1 in the $Y_{MSO} - Z_{MSO}$ plane. **(c, d, e)** depict the H^+ (hydrogen ions), O^+ , and O_2^+ energy spectrum measured by Suprathermal and Thermal Ion Composition (STATIC)⁵³. **f** Shows the number density of H^+ , O^+ , and O_2^+ . **g** Display the tailward speed of O^+ and O_2^+ . **h** Displays the time series of magnetic field vectors in MSO coordinates measured by magnetometer (MAG)⁵⁴. The gray shaded area highlights the interval of the analyzed event (13:26:00–13:27:30).

Under the condition where the upstream IMF has a clock angle of 228.5° and assuming that the solar wind velocity is purely along the tailward direction, the $\mathbf{X}_{MSE} = (1, 0, 0)$, $\mathbf{Y}_{MSE} = (0, -0.75, -0.66)$, $\mathbf{Z}_{MSE} = (0, 0.66, -0.75)$. Thus, the orientations of the \mathbf{Y}_{MSE} and \mathbf{Z}_{MSE} represent a 138.6° counterclockwise rotation relative to the \mathbf{Y}_{MSO} and \mathbf{Z}_{MSO} . Figure 2h shows the projection of the locations of MAVEN and Tianwen-1 in the $Y_{MSE} - Z_{MSE}$ plane, revealing Tianwen-1's placement on the $+Y_{MSE}$ flank side, whereas MAVEN is positioned on the $-Y_{MSE}$ side, nearing the anticipated center of draped field lines⁴¹. According to the pattern of the induced magnetosphere (see Fig. 2i), this spatial arrangement suggests that at Tianwen-1's location, the $B_{X_{MSO}}$ component is expected to be negative, while at MAVEN's position, $B_{X_{MSO}}$ is predicted to be close to zero. These predictions align well with the observations detailed in Fig. 2a, b, further confirming the reliability of the MSE coordinates. Surprisingly, contrary to our expectation, Fig. 2h shows that MAVEN was actually positioned in the polar region of the $-Z_{MSE}$ hemisphere (-E hemisphere), which is unexpected according to current theories.

The magnetic fields also exhibited atypical variations. During the period from 13:25:58 to 13:26:06, highlighted by a yellow shaded interval in Fig. 2a–c, MAVEN recorded significant deviations in the clock angle of the magnetic field compared to other times, with

detailed views provided in Fig. 2d–g. Contrary to the expected behavior where the $B_{Y_{MSE}}$ components should remain positive and the clock angle should remain steady under relatively stable solar wind conditions, we observed that the $B_{Y_{MSE}}$ components reverse to negative during two short intervals (see the blue areas in Fig. 2f), along with four distinct variations in the clock angle at 13:26:01.1, 13:26:01.6, 13:26:02.2, and 13:26:03.8 (Fig. 2g), which are indicated by black vertical dashed lines. A possible cause of these unusual magnetic field variations, including the reversal of $B_{Y_{MSE}}$ and significant fluctuations in the clock angle, is an IMF discontinuity, which globally alters the configuration of the induced magnetosphere. However, as we mentioned before, the steady magnetic fields observed by Tianwen-1 indicate that the upstream solar wind conditions are relatively stable. Therefore, it is suggested that MAVEN detected spatially localized magnetic field structures, whereas Tianwen-1 did not.

Unexpected motion of escaping ions

In addition to the unexpected location and the magnetic fields, the motion of these ions also exhibits unusual properties. Figure 3a, b displays the bulk velocities of O^+ and O_2^+ in the MSE frame, showing a predominant tailward motion for both ion species. Interestingly, the $V_{Z_{MSE}}$ components for both O^+ and O_2^+ start negative, shift to positive

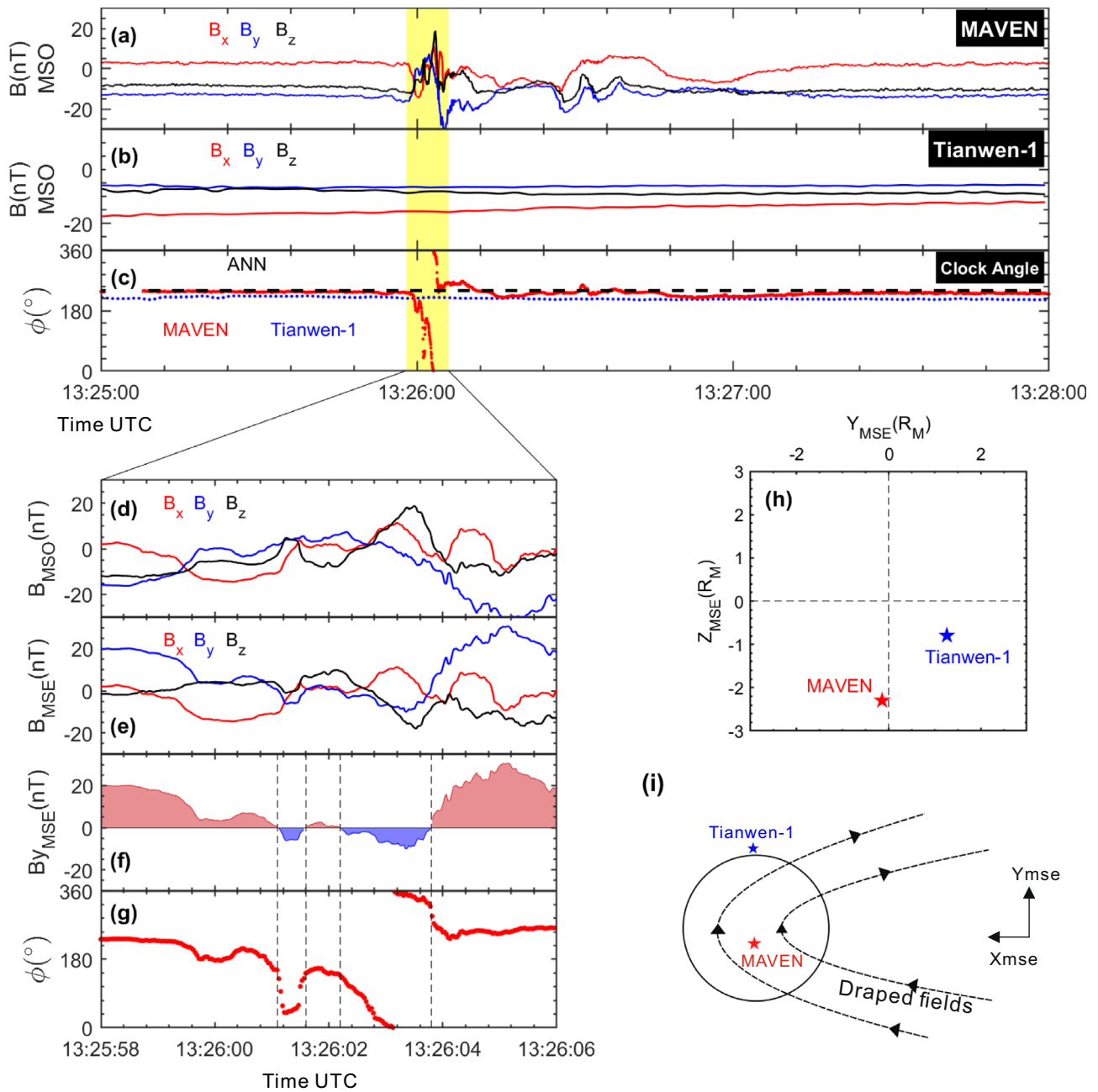


Fig. 2 | Magnetic field measurements during September 23, 2022. **a** Display the magnetic fields in MSO coordinates as observed by MAVEN. **b** shows the magnetic fields measured by the Mars Orbiter Magnetometer (MOMAG) onboard Tianwen-1^{55–58}, respectively. **c** Compares the clock angle of the magnetic field between observations from MAVEN and Tianwen-1, and the upstream IMF as derived from an artificial neural network (ANN). The yellow shaded area in (a–c) highlights the interval of the fluctuating magnetic field with significant deviations in clock angle.

d, e present a zoomed-in view of the magnetic field observations by MAVEN in MSO and MSE coordinates from 13:25:58 to 13:26:06. **f, g** Display the $B_{y_{MSE}}$ clock angle measured by MAVEN. The red (blue) area denotes the $+B_{y_{MSE}}$ ($-B_{y_{MSE}}$). The four dashed lines highlight the four reversals of $B_{y_{MSE}}$ components and significant changes in clock angle. **h** Illustrates the projection of MAVEN and Tianwen-1’s averaged locations on the $Y_{MSE} - Z_{MSE}$ plane. **i** Provides a sketch of the classical induced magnetic field configuration.

by 13:26:30, then rapidly revert to negative, and finally return to positive by 13:27:00. These transitions are further illustrated in Fig. 3c, d, which depict the reduced two-dimensional velocity distributions of O_2^+ in the $V_{x_{MSE}} - V_{z_{MSE}}$ plane. The majority of O_2^+ ions were found at a $V_{z_{MSE}}$ of -100 km/s at 13:26:08 (Fig. 3c), and $+80$ km/s at 13:27:16 (Fig. 3d). The velocity distribution of oxygen ions shown in Fig. 3d is significantly different from the observed and simulated velocity distributions of ionospheric ions in the terminator region, where high-energy ionospheric ions typically exhibit positive $V_{z_{MSE}}$ values^{18,20,42}.

Discussion

We report the observations of anomalous transient enhancements of ionospheric ion escape at Mars. The main findings from the observations can be summarized as follows:

First, we observed a transient appearance of ionospheric ions escaping into space, characterized by high energies and fluxes (10–100 times higher than the average observed in other primary escape channels), indicating a bursty escape. Interestingly, these ionospheric ions exhibited atypical signatures regarding their locations. Specifically, they were detected in an unexpected region, the

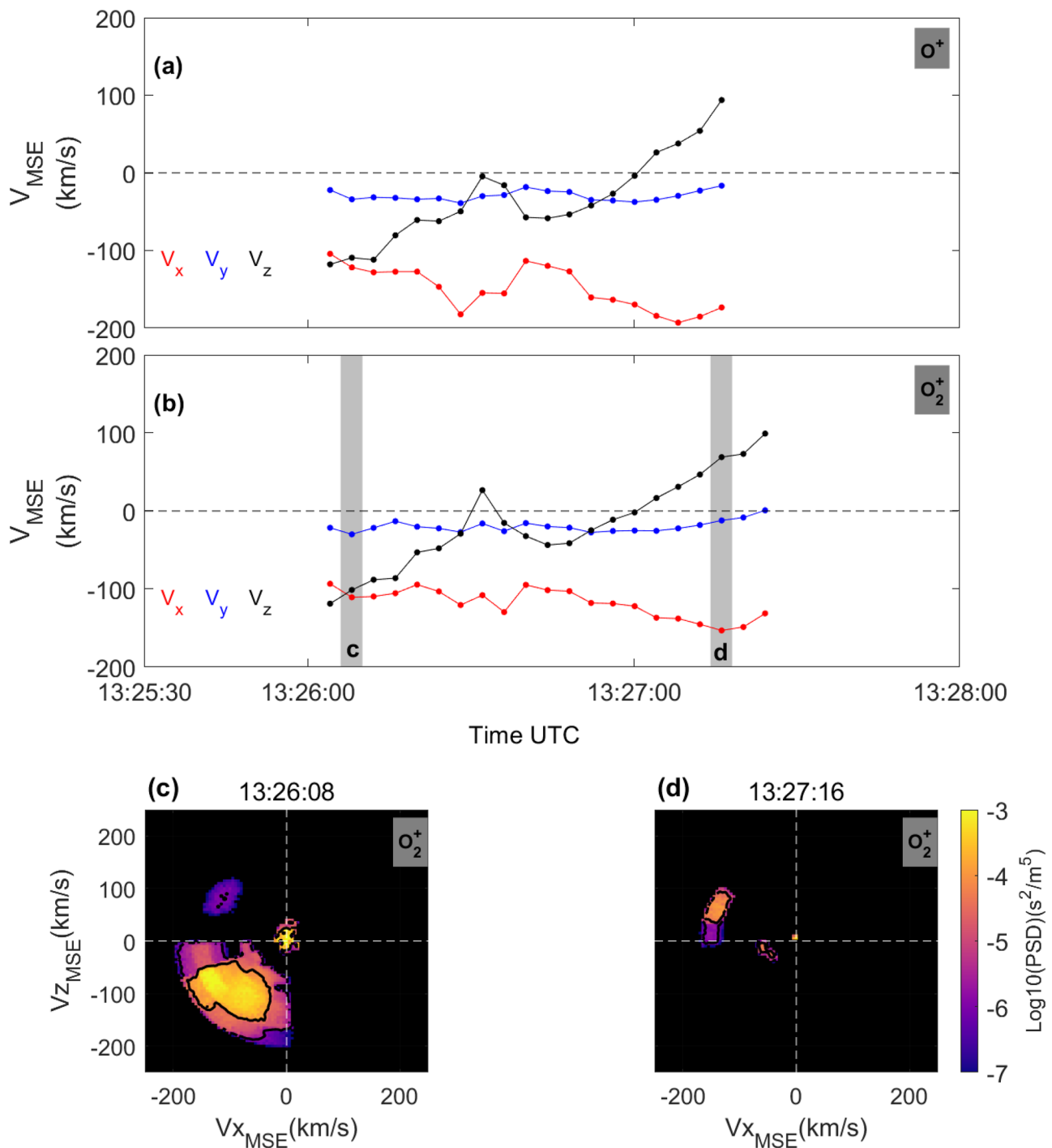


Fig. 3 | STATIC observations of the motion of ions during 13:25:30–13:28:00 UTC September 23, 2022. **a, b** display the bulk velocities of O^+ and O_2^+ in the MSE frame, respectively. The grey shaded regions in **(b)**, marked with the labels “c”, “d”

correspond to the time intervals for the velocity distributions shown in **(c, d)**. These panels illustrate the measured velocity distributions of O_2^+ in the $V_{x,MSE} - V_{z,MSE}$ plane at the times 13:26:08, and 13:27:16, respectively.

–E hemisphere, where they generally struggle to gain sufficient energy and are more likely to return to the atmosphere rather than escape into space.

Second, concurrent with these transient ionospheric ions, MAVEN observed spatially localized magnetic field structures that significantly alter the local magnetic field, deviating from the expected pattern of the induced magnetosphere. However, Tianwen-1 did not detect these spatially localized magnetic field structures but instead detected a stable magnetic field. This suggests that the external solar wind conditions did not change significantly during this event.

The observation indicates that ionospheric ions in the –E hemisphere can transiently behave like those in the +E hemisphere, gaining sufficient energy to escape into space, resulting in a bursty escape of ionospheric ions. Based on multi-point observations, we suggest that such events are not caused by the variation of external solar wind. Therefore, planetary ion escape is highly dynamic and could exhibit both temporal and spatial variabilities even under relatively steady external conditions, warranting further investigation through current and future multi-point observations. These findings also raise several questions: How did the ionospheric ions manage to gain such high

energy and migrate into the high-altitude region of the -E hemisphere? What are these spatially localized structures, and what is their relationship with these anomalous escaping ions?

Possible mechanism

Previous studies have suggested that, apart from variations in the external solar wind, the bursty escape of ionospheric ions may be triggered by magnetic flux ropes generated through crustal field reconnection²⁵ and the snowplow effect in the boundary²⁷. However, in our observations, the magnetic field characteristics do not align with those of magnetic flux ropes, nor did our event occur in the downstream region of the crustal fields. Moreover, the escaping ions we observed exhibit energetic characteristics, with energies ranging from 1 keV to 6 keV, that cannot be explained by either the snowplow effect or magnetic flux ropes. Consequently, alternative mechanisms should be considered to explain the observed anomalous ion escape.

Considering that these ionospheric ions that are observed in the -E (-Z_{MSE}) hemisphere have a negative value of V_{Z_{MSE}} components, it is suggested that these ions were initially accelerated along the -E direction or the direction of -Z_{MSE}, and migrated to the -E hemisphere. If the ionospheric ions start with zero velocity and are subsequently accelerated by the electric fields, their V_{Z_{MSE}} can be roughly estimated as:

$$V_{Z_{MSE}} = \begin{cases} \sqrt{\frac{2q}{m} \int E_{Z_{MSE}} \cdot dZ_{MSE}} & \text{if } \int E_{Z_{MSE}} \cdot dZ_{MSE} > 0, \\ -\sqrt{\frac{2q}{m} \left| \int E_{Z_{MSE}} \cdot dZ_{MSE} \right|} & \text{if } \int E_{Z_{MSE}} \cdot dZ_{MSE} < 0 \end{cases} \quad (1)$$

where m and q represent the mass and electric charge of the ions, respectively. The $E_{Z_{MSE}}$ denotes the components of the electric field along the Z_{MSE}. Since Hall electric fields and ambipolar electric fields are generally small compared to the convective electric field and typically do not energize ions to above 1 keV in the dayside region^{41,43}, we only consider the convective electric field here. Thus, $E_{Z_{MSE}}$ could be estimated as $-V_{X_{MSE}} \cdot B_{Y_{MSE}}$, where $V_{X_{MSE}}$ represents the components of the solar wind velocity along the X_{MSE}. Therefore, the Eq. (1) can also be expressed as:

$$V_{Z_{MSE}} = \begin{cases} \sqrt{\frac{2q}{m} \int -V_{X_{MSE}} \cdot B_{Y_{MSE}} \cdot dZ_{MSE}} & \text{if } \int V_{X_{MSE}} \cdot B_{Y_{MSE}} \cdot dZ_{MSE} < 0 \\ -\sqrt{\frac{2q}{m} \int V_{X_{MSE}} \cdot B_{Y_{MSE}} \cdot dZ_{MSE}} & \text{if } \int V_{X_{MSE}} \cdot B_{Y_{MSE}} \cdot dZ_{MSE} > 0 \end{cases} \quad (2)$$

From Eq. (2), it is evident that the V_{Z_{MSE}} are linked with B_{Y_{MSE}}. Based on this, we can simply describe the relationship between the localized magnetic field structures and the observed anomalous transient ionospheric ions through the following physical process: Initially, before the arrival of these localized magnetic structures, B_{Y_{MSE}} was positive throughout the magnetosheath region, resulting in a positive E_{Z_{MSE}}. Therefore, ions generated in the -E hemisphere were accelerated back toward the planet, making it difficult for them to gain energy and move to high-altitude regions. Consequently, MAVEN could not detect high-energy ionospheric ions before this event. However, as these localized structures carried the -B_{Y_{MSE}} and -E_{Z_{MSE}} moved downstream and encountered the ionospheric ions, the ions would be accelerated in the -Z_{MSE} direction. This caused the ionospheric ions generated in the -E hemisphere to gain energy and migrate to the high-altitude region. Consequently, MAVEN detected the sudden emergence of these high-energy ionospheric ions, most of which exhibit negative -V_{Z_{MSE}} values. As these ions exited the structures, they decelerated (or accelerated) along the -Z_{MSE} (+Z_{MSE}) direction. As a result, MAVEN was observed V_{Z_{MSE}} gradually turning positive (see Fig. 3b). Finally, as these localized structures passed by or dissipated, the acceleration and motion of ionospheric ions returned to the classical pattern. Thus, these ions became undetectable by MAVEN again. These processes could well explain why MAVEN observed transient ionospheric ions with negative V_{Z_{MSE}} values in the -E hemisphere. Thus, we suggest the spatially

localized structures create a temporary and efficient channel for the energization and escape of ionospheric ions in the -E hemisphere, causing them to act similarly to the ionospheric ions in the +E hemisphere.

The next question is: what are these spatially localized structures? From Fig. 4, we observe that as MAVEN transitions from the downstream undisturbed region to the “-B_{Y_{MSE}}” region, there is a slight decrease in magnetic field strength (see Fig. 4a) and an increase in the temperature of solar wind H⁺ (see Fig. 4c). As MAVEN approaches the upstream edge, there is a significant increase in both the magnetic field strength and the total number density of ions (see Fig. 4b). These characteristics are consistent with those of foreshock transients, which typically feature a compressional shock at the upstream edge, marked by enhanced ion density and magnetic field strength, and a core region characterized by depressed and fluctuating magnetic fields^{44–51}. Furthermore, the solar wind is generally deflected, depleted, and heated in foreshock transients, which is also consistent with our observations. Therefore, we propose that these spatially localized magnetic structures are foreshock transients that modify the electromagnetic fields and subsequently influence the motion of ionospheric ions. Given that Tianwen-1 did not detect it, the spatial extent of the foreshock transients along the trajectory between Tianwen-1 and MAVEN must be shorter than the distance that separates them, approximately 7000 km or 2.1 R_M.

In summary, we propose that the foreshock introduces additional temporal and spatial variabilities to the solar wind, thereby making ion escape at Mars more complex and dynamic. Given its consistent presence, irrespective of solar conditions⁵², we suggest that the foreshock likely plays a significant role in ion escape at Mars, a factor that has previously been overlooked.

Methods

Instruments

Here we adopt ion data from the Suprathermal, Thermal Ion Composition (STATIC) instrument⁵³, and magnetic field measurements from the Magnetometer (MAG)⁵⁴, onboard MAVEN. The MAG is a fluxgate magnetometer that measures three-dimensional magnetic field vectors at a frequency of 32 Hz. We also use the c6 and d1 data of STATIC that provides the omni spectrum and three-dimensional velocity distributions of H⁺, O⁺, and O₂⁺ with energy between 0 and 30 keV/q at time resolution of 4 s. STATIC consists of a time-of-flight sensor which can measure the mass-per-charge of ions and then determine the ion species. The field-of-view of STATIC is 360° × 90°. In addition to MAVEN, we use the magnetic field data measured by the Tianwen-1 Mars Orbiter Magnetometer (MOMAG)^{55–58}. The MOMAG could measure the three-dimensional magnetic field vectors at a frequency of 128 Hz. For our analysis, we use data products that are provided at a time resolution of 1 Hz.

MSO and MSE coordinates

We employed two Cartesian coordinate systems. The first is the Mars Solar Orbital (MSO) coordinates⁵⁹. Here, X_{MSO} is along the vector from Mars to the Sun, Z_{MSO} is perpendicular to the orbital plane, and Y_{MSO} completes the right-handed system, closely aligned with the opposite direction of the orbital velocity vector. Given that the configuration of the induced magnetosphere is influenced by the solar wind and IMF orientation, we have also adopted a second coordinate system, the Mars Solar Electric (MSE) coordinates. In this system, X_{MSE} is anti-parallel to the upstream solar wind velocity, Z_{MSE} aligns with the direction of the upstream solar wind convective electric field (E_{SW}), and Y_{MSE} completes the right-handed system, aligning with the cross-flow magnetic field component of the interplanetary magnetic field (IMF). Here, we assume that X_{MSE} is same to the X_{MSO}.

Magnetic pile-up boundary

The magnetic pileup boundary (MPB) is a plasma boundary that separates the magnetosheath, a region of weak and fluctuating

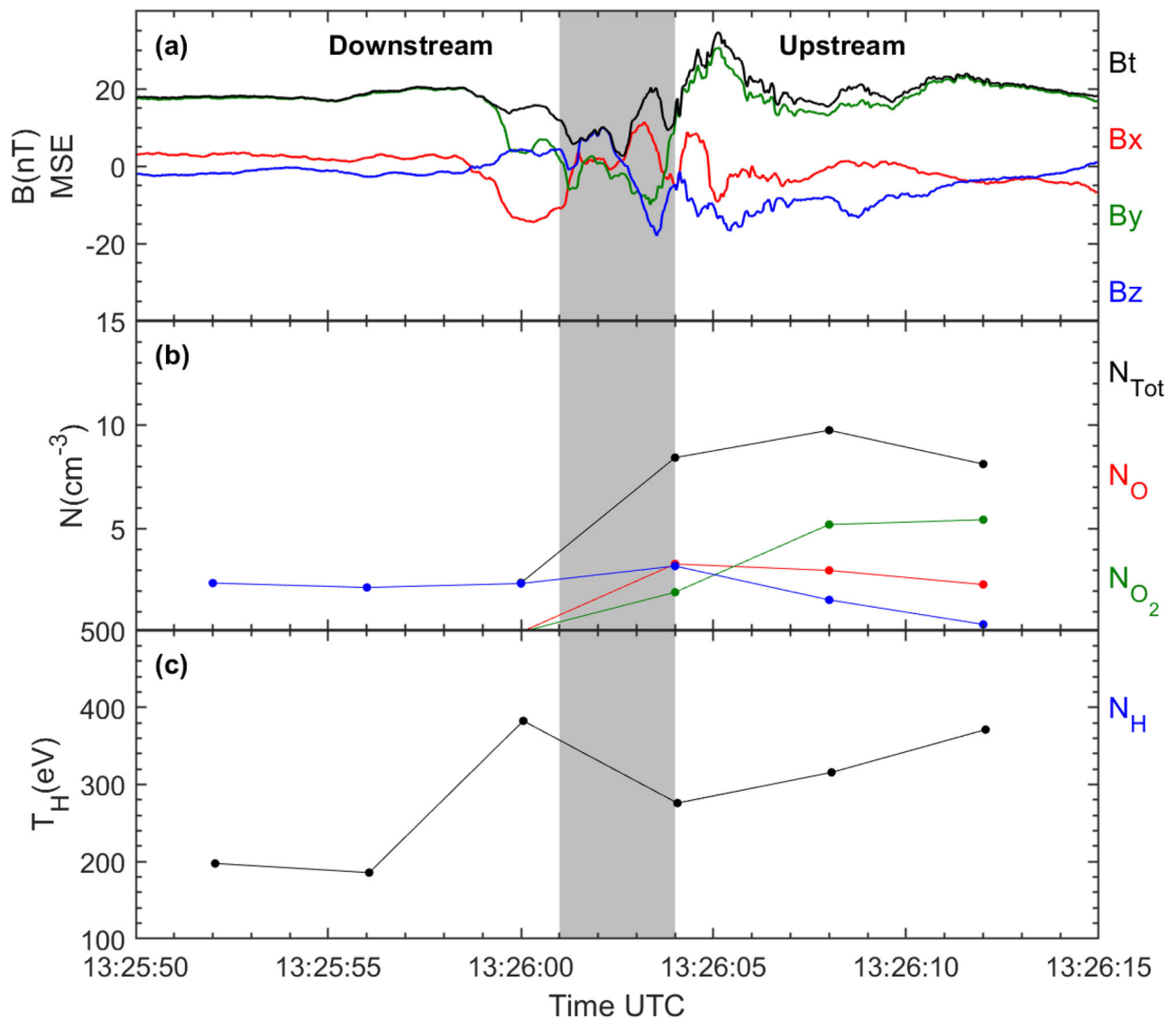


Fig. 4 | Magnetic field and ion measurements of the spatially localized structure during September 23, 2022. a Magnetic fields. **b** Ion density. The N_{Tot} denotes the total ion density, which is calculated as $N_{Tot} = N_{H^+} + N_{O^+} + N_{O_2^+}$, where N_{H^+} , N_{O^+}

and $N_{O_2^+}$ represent the density of H^+ , O^+ , and O_2^+ . **c** Temperature of solar wind protons. The grey shaded area indicates the interval of “ $-By_{MSE}$ ”.

magnetic fields, from an inner region dominated by enhanced and well-organized magnetic fields due to draping of the IMF over a conducting obstacle.

Moment calculation

We calculate the density and velocity of ions using the integrated method^{14,60,61}. Assuming the phase space density of ions can be represented by f , the density n can be calculated as:

$$n = \int d\varphi \int \cos(\theta) d\theta \int v^2 f dv \quad (3)$$

where θ , φ are the elevation and azimuth angles in the STATIC spherical coordinates, v represents the speed of ions. The velocity components of ions can be estimated as:

$$\begin{aligned} V_x &= \int \cos(\varphi) d\varphi \int \cos^2(\theta) d\theta \int v^3 f dv / n \\ V_y &= \int \sin(\varphi) d\varphi \int \cos^2(\theta) d\theta \int v^3 f dv / n \\ V_z &= \int d\varphi \int \cos(\theta) \sin(\theta) d\theta \int v^3 f dv / n \end{aligned} \quad (4)$$

where V_x , V_y , and V_z represent the x , y , and z components of velocity in STATIC coordinates. These can then be transformed into MSO or MSE coordinates. The tailward escaping flux of each ion can be estimated as:

$$F = n \cdot V_{x,ms0} \quad (5)$$

where $V_{x,ms0}$ represents the x component of the velocity in MSO coordinates.

Data availability

All data used in this paper are public. The MAVEN MAG data is publicly archived at <https://pds-ppi.igpp.ucla.edu/mission/MAVEN/Magnetometer>⁶². The MAVEN STATIC data is publicly archived at https://pds-ppi.igpp.ucla.edu/mission/MAVEN/Supra-Thermal_and_Thermal_Ion_Composition⁶³. The Tianwen-1 MOMAG data sets are publicly available at <https://moon.bao.ac.cn/web/zhmanager/mars1> and http://space.ustc.edu.cn/dreams/tw1_momag/. The datasets generated during and/or analyzed during the current study are available from the Zenodo repository (<https://doi.org/10.5281/>

zenodo.14941994). The source data files for the figures in this current study have been deposited in Zenodo repository (<https://doi.org/10.5281/zenodo.15032394>). Source data are provided with this paper⁶⁴. Source data are provided with this paper.

Code availability

Both MAVEN and Tianwen-1 data are primarily analyzed and plotted using the IRFU-Matlab software (<https://github.com/irfu/irfu-matlab>)⁶⁵ and SPEDAS⁶⁶.

References

- Hurowitz, J. A. et al. Redox stratification of an ancient lake in Gale Crater, Mars. *Science* **356**. <https://doi.org/10.1126/science.aah6849> (2017).
- Hynek, B. M., Beach, M. & Hoke, M. R. T. Updated global map of Martian valley networks and implications for climate and hydrologic processes. *J. Geophys. Res.* **115**, E09008 (2010).
- Lillis, R. J., Robbins, S., Manga, M., Halekas, J. S. & Frey, H. V. Time history of the Martian dynamo from crater magnetic field analysis. *J. Geophys. Res. Planets* **118**, 1488–1511 (2013).
- Brain, D. A. et al. The spatial distribution of planetary ion fluxes near Mars observed by MAVEN. *Geophys. Res. Lett.* **42**, 9142–9148 (2015).
- Dong, C. et al. Modeling martian atmospheric losses over time: implications for exoplanetary climate evolution and habitability. *Astrophys. J.* **859**. <https://doi.org/10.3847/2041-8213/aac489> (2018).
- Dong, C. et al. Solar wind interaction with Mars upper atmosphere: results from the one-way coupling between the multifluid MHD model and the MTGCM model. *Geophys. Res. Lett.* **41**, 2708–2715 (2014).
- Jakosky, B. et al. MAVEN observations of the response of Mars to an interplanetary coronal mass ejection. *Science* **350**. <https://doi.org/10.1126/science.aad0210> (2015).
- Jakosky, B. M. et al. Loss of the Martian atmosphere to space: present-day loss rates determined from MAVEN observations and integrated loss through time. *Icarus* **315**, 146–157 (2018).
- Ramstad, R., Barabash, S., Futaana, Y., Nilsson, H. & Holmström, M. Ion escape from Mars through time: an extrapolation of atmospheric loss based on 10 years of Mars express measurements. *J. Geophys. Res. Planets* **123**, 3051–3060 (2018).
- Nilsson, H. et al. Solar cycle variation of ion escape from Mars. *Icarus* <https://doi.org/10.1016/j.icarus.2021.114610> (2021).
- Barabash, S., Fedorov, A., Lundin, R., & Sauvaud, J. Martian atmospheric erosion rates. *Nature* **315**. <https://doi.org/10.1126/science.1134358> (2007).
- Lundin, R., Zakharov, A., Pellinen, R., Borg, H., & Hultqvist, B. First measurements of the ionospheric plasma escape from Mars. *Nature*. <https://doi.org/10.1038/341609a0> (1989).
- Zhang, C. et al. MAVEN observations of periodic low-altitude plasma clouds at Mars. *Astrophys. J. Lett.* **922**. <https://doi.org/10.3847/2041-8213/ac3a7d> (2021).
- Zhang, C. et al. Mars-Ward ion flows in the Martian magnetotail: Mars express observations. *Geophys. Res. Lett.* **49**. <https://doi.org/10.1029/2022gl100691> (2022).
- Zhang, C. et al. The energetic oxygen ion beams in the Martian magnetotail current sheets: hints from the comparisons between two types of current sheets. *Geophys. Res. Lett.* **51**. <https://doi.org/10.1029/2023gl107190> (2024).
- Dong, C. et al. Multifluid MHD study of the solar wind interaction with Mars' upper atmosphere during the 2015 March 8th ICME event. *Geophys. Res. Lett.* **42**, 9103–9112 (2015).
- Jarvinen, R., Brain, D. A., Modolo, R., Fedorov, A. & Holmström, M. Oxygen ion energization at Mars: comparison of MAVEN and Mars express observations to global hybrid simulation. *J. Geophys. Res. Space Phys.* **123**, 1678–1689 (2018).
- Fang, X. et al. Pickup oxygen ion velocity space and spatial distribution around Mars. *J. Geophys. Res. Space Phys.* **113**. <https://doi.org/10.1029/2007ja012736> (2008).
- Fang, X., Liemohn, M. W., Nagy, A. F., Luhmann, J. G. & Ma, Y. Escape probability of Martian atmospheric ions: controlling effects of the electromagnetic fields. *J. Geophys. Res. Space Phys.* **115**. <https://doi.org/10.1029/2009JA014929> (2010).
- Dong, Y. et al. Strong plume fluxes at Mars observed by MAVEN: an important planetary ion escape channel. *Geophys. Res. Lett.* **42**, 8942–8950 (2015).
- Halekas, J. S., Ruhunusiri, S., McFadden, J. P., Espley, J. R. & DiBraccio, G. A. Ion composition boundary layer instabilities at Mars. *Geophys. Res. Lett.* **46**, 10303–10312 (2019).
- Ma, X. et al. Tianwen-1 and MAVEN observations of Martian oxygen ion plumes. *Icarus* **406**. <https://doi.org/10.1016/j.icarus.2023.115758> (2023).
- Sakakura, K. et al. Formation mechanisms of the molecular ion polar plume and its contribution to ion escape from Mars. *J. Geophys. Res. Space Phys.* **127**. <https://doi.org/10.1029/2021ja029750> (2022).
- Qiao, F. et al. Acceleration of pick-up ions in the Martian magnetosheath: a Tianwen-1 case study. *J. Geophys. Res. Space Phys.* **129**, e2024JA032461 (2024).
- Brain, D. A. et al. Episodic detachment of Martian crustal magnetic fields leading to bulk atmospheric plasma escape. *Geophys. Res. Lett.* **37**. <https://doi.org/10.1029/2010gl043916> (2010).
- Dubinin, E. et al. Bursty ion escape fluxes at Mars. *J. Geophys. Res. Space Phys.* **126**. <https://doi.org/10.1029/2020ja028920> (2021).
- Halekas, J. S. et al. Plasma clouds and snowplows: bulk plasma escape from Mars observed by MAVEN. *Geophys. Res. Lett.* **43**, 1426–1434 (2016).
- Eastwood, J. P. et al. The foreshock. *Space Sci. Rev.* **118**, 41–94 (2005).
- Mazelle, C. et al. Bow shock and upstream phenomena at Mars. *Space Sci. Rev.* **111**. <https://doi.org/10.1023/B:SPAC.0000032717.98679.d0> (2004).
- Lillis, R. J. et al. ESCAPE: a twin spacecraft simplex mission to Unveil Mars' Unique Hybrid Magnetosphere. In *Proc. 53rd Lunar and Planetary Science Conference LPI Contributions* (p. 1135). volume 2678 of LPI Contributions (2022).
- Sanchez-Cano, B. & The M-MATISSE team. The M-MATISSE mission: Mars Magnetosphere ATmosphere Ionosphere and Space weather SciencE. An ESA Medium class (M7) candidate, In *Proc. EGU General Assembly 2023*, Vienna, Austria, 24–28 Apr 2023, EGU23-13687, <https://doi.org/10.5194/egusphere-egu23-13687> (2023).
- Jakosky, B. M. et al. The Mars Atmosphere and Volatile Evolution (MAVEN) mission. *Space Sci. Rev.* **195**, 3–48 (2015).
- Wan, W. X., Wang, C., Li, C. L. & Wei, Y. China's first mission to Mars. *Nat. Astron.* **4**, 721 (2020).
- Inui, S. et al. Statistical study of heavy ion outflows from Mars observed in the Martian-induced magnetotail by MAVEN. *J. Geophys. Res. Space Phys.* **124**, 5482–5497 (2019).
- Modolo, R., Chanteur, G. M. & Dubinin, E. Dynamic Martian magnetosphere: transient twist induced by a rotation of the IMF. *Geophys. Res. Lett.* **39**. <https://doi.org/10.1029/2011gl049895> (2012).
- Romanelli, N. et al. Recovery timescales of the dayside martian magnetosphere to IMF variability. *Geophys. Res. Lett.* **46**, 10977–10986 (2019).

37. Romanelli, N. et al. Responses of the Martian magnetosphere to an interplanetary coronal mass ejection: MAVEN observations and LatHyS results. *Geophys. Res. Lett.* **45**, 7891–7900 (2018).
38. Hurley, D. M., Dong, Y., Fang, X. & Brain, D. A. A proxy for the upstream IMF clock angle using MAVEN magnetic field data. *J. Geophys. Res. Space Phys.* **123**, 9612–9618 (2018).
39. Dong, Y. et al. Magnetic field in the Martian magnetosheath and the application as an IMF Clock angle proxy. *J. Geophys. Res. Space Phys.* **124**, 4295–4313 (2019).
40. Ruhunusiri, S. et al. An artificial neural network for inferring solar wind proxies at Mars. *Geophys. Res. Lett.* **45**. <https://doi.org/10.1029/2018gl079282> (2018).
41. Zhang, C. et al. Three-dimensional configuration of induced magnetic fields around Mars. *J. Geophys. Res. Planets* **127**. <https://doi.org/10.1029/2022je007334> (2022).
42. Dubinin, E. et al. Induced magnetic fields and plasma motions in the inner part of the Martian magnetosphere. *J. Geophys. Res. Space Phys.* **126**. <https://doi.org/10.1029/2021ja029542> (2021).
43. Xu, S. et al. Field-aligned potentials at Mars from MAVEN observations. *Geophys. Res. Lett.* **45**, 10,119–110,127 (2018).
44. Collinson, G. et al. A hot flow anomaly at Mars. *Geophys. Res. Lett.* **42**, 9121–9127 (2015).
45. Collinson, G. et al. Spontaneous hot flow anomalies at Mars and Venus. *J. Geophys. Res. Space Phys.* **122**, 9910–9923 (2017).
46. Madanian, H. et al. Transient foreshock structures upstream of Mars: implications of the small martian bow shock. *Geophys. Res. Lett.* **50**. <https://doi.org/10.1029/2022gl101734> (2023).
47. Shestakov, A. Y., & Shuvalov, S. D. Planetary ions acceleration in a hot flow anomaly at Mars. *Planetary Space Sci.* **237**. <https://doi.org/10.1016/j.pss.2023.105781> (2023).
48. Shuvalov, S. D., Ermakov, V. N., Zorina, V. O., & Kim, K. I. Propagation properties of hot flow anomalies at Mars: MAVEN observations. *Planetary Space Sci.* **179**. <https://doi.org/10.1016/j.pss.2019.104717> (2019).
49. Zhang, H. et al. Dayside transient phenomena and their impact on the magnetosphere and ionosphere. *Space Sci. Rev.* **218**, 40 (2022).
50. Liu, T. Z., Angelopoulos, V., Hietala, H. & Wilson Iii, L. B. Statistical study of particle acceleration in the core of foreshock transients. *J. Geophys. Res. Space Phys.* **122**, 7197–7208 (2017).
51. Liu, T. Z. et al. Statistical study of foreshock transients in the midtail foreshock. *J. Geophys. Res. Space Phys.* **126**. <https://doi.org/10.1029/2021ja029156> (2021).
52. Yamauchi, M. et al. Oxygen foreshock of Mars. *Planet. Space Sci.* **119**, 48–53 (2015).
53. McFadden, J. et al. MAVEN suprathermal and thermal ion composition (STATIC) instrument. *Space Sci. Rev.* **195**, 199–256 (2015).
54. Connerney, J. et al. The MAVEN magnetic field investigation. *Space Sci. Rev.* **195**, 257–291 (2015).
55. Wang, Y. et al. The Mars orbiter magnetometer of Tianwen-1: in-flight performance and first science results. *Earth Planet. Phys.* **7**, 1–13 (2023).
56. Zou, Z. et al. In-flight calibration of the magnetometer on the Mars Orbiter of Tianwen-1. *Sci. China Technol. Sci.* **66**, 2396–2405 (2023).
57. Liu, K. et al. Mars orbiter magnetometer of China’s First Mars Mission Tianwen-1. *Earth Planet. Phys.* **4**, 384–389 (2020).
58. Wang, G. Q. et al. Calibration of the zero offset of the fluxgate magnetometer on board the Tianwen-1 orbiter in the Martian magnetosheath. *J. Geophys. Res. Space Phys.* **129**, e2023JA031757 (2024).
59. Zhang, C. et al. Properties of flapping current sheet of the Martian magnetotail. *J. Geophys. Res. Space Phys.* **128**. <https://doi.org/10.1029/2022ja031232> (2023).
60. Fränz, M. et al. Plasma moments in the environment of Mars. *Space Sci. Rev.* **126**, 165–207 (2006).
61. Fowler, C. M. et al. In-situ measurements of ion density in the martian ionosphere: underlying structure and variability observed by the MAVEN-STATIC instrument. *J. Geophys. Res. Space Phys.* **127**. <https://doi.org/10.1029/2022ja030352> (2022).
62. Connerney, J. E. P. MAVEN magnetometer (MAG) calibrated data bundle. NASA Planetary Data System. *Space Sci. Rev.* <https://doi.org/10.17189/1414178> (2023).
63. McFadden, J. P. MAVEN suprathermal and thermal ion composition (STATIC) calibrated data bundle. *NASA Planet. Data Syst.* <https://doi.org/10.17189/1517741> (2023).
64. Zhang, C. Source dataset for “anomalous transient enhancement of planetary ion escape at Mars”. Zenodo. <https://doi.org/10.5281/zenodo.15032394> (2025).
65. Khotyaintsev, Y. et al. irfu/irfu-matlab: v1.16.3 (v1.16.3). Zenodo. <https://doi.org/10.5281/zenodo.11550091> (2022).
66. Angelopoulos, V. et al. The space physics environment data analysis system (SPEDAS). *Space Sci. Rev.* **215**, 9 (2019).
67. Trotignon, J. G., Mazelle, C., Bertucci, C. & Acuña, M. H. Martian shock and magnetic pile-up boundary positions and shapes determined from the Phobos 2 and Mars Global Surveyor data sets. *Planet. Space Sci.* **54**, 357–369 (2006).

Acknowledgements

This work was partially supported by NASA grant NNH10CC04C through the MAVEN Project, NASA grants 80NSSC23K0911 (C. D.) and 80NSSC24K1843 (C. D.), and the Alfred P. Sloan Research Fellowship (C. D.). We thank the MAVEN and Tianwen-1 instrument teams for working to provide the data. We acknowledge fruitful discussions with James P. McFadden.

Author contributions

All of the authors made notable contributions to this work. C.Z. and C.D. conceived this study. C.Z., C.D., H.Z., Y.C., J.H., H.N., T.L., M.Y., S.X., Y.D., M.P., Y.D., M.Z., R.R., S.R., C.M., M.H. and C.L. carried out the data analysis, interpretation and manuscript preparation. S.C. reviewed and provided feedback on the paper and is also the leader of the MAVEN mission. K.G.H. contributed to the data calibration and background count removal for STATIC. All authors contributed to the discussion, and read and commented on the manuscript.

Competing interests

The authors declare no competing interests.

Additional information

Supplementary information The online version contains supplementary material available at <https://doi.org/10.1038/s41467-025-58351-y>.

Correspondence and requests for materials should be addressed to Chi Zhang or Chuanfei Dong.

Peer review information *Nature Communications* thanks Matthew Fillingim, and the other, anonymous, reviewer for their contribution to the peer review of this work. A peer review file is available.

Reprints and permissions information is available at <http://www.nature.com/reprints>

Publisher’s note Springer Nature remains neutral with regard to jurisdictional claims in published maps and institutional affiliations.

Open Access This article is licensed under a Creative Commons Attribution-NonCommercial-NoDerivatives 4.0 International License, which permits any non-commercial use, sharing, distribution and reproduction in any medium or format, as long as you give appropriate credit to the original author(s) and the source, provide a link to the Creative Commons licence, and indicate if you modified the licensed material. You do not have permission under this licence to share adapted material derived from this article or parts of it. The images or other third party material in this article are included in the article's Creative Commons licence, unless indicated otherwise in a credit line to the material. If material is not included in the article's Creative Commons licence and your intended use is not permitted by statutory regulation or exceeds the permitted use, you will need to obtain permission directly from the copyright holder. To view a copy of this licence, visit <http://creativecommons.org/licenses/by-nc-nd/4.0/>.

© The Author(s) 2025